

Supplementary Information

The framework for our computational enzyme design approach is structured across four hierarchical levels, each of which builds upon the outcomes of the previous stage, forming a top-down operation (Figure S1). These stages consist of protein preparation, mutant generation, geometry variation, and the energy engine. Each level focuses on different aspects of the enzyme optimization process, contributing to the overall refinement of enzyme performance.

The first level, protein preparation, involves constructing computational models for known enzyme structures, which can be derived from X-ray crystallography data or computational predictions using advanced tools like AlphaFold3 and RoseTTAFold2. These models represent a diverse array of enzyme types, incorporating various substrates, sequences, cofactors, coenzymes, and protonation states, as well as factors like stoichiometry and structure quality (e.g., the presence of missing loops or hydrogen atoms). This foundational step ensures that the enzyme structure is accurately represented before modifications are made, providing a reliable starting point for subsequent stages.

The next level, mutant generation, focuses on the creation of enzyme variants based on a common enzyme scaffold. In this step, mutations are introduced to the enzyme's amino acid sequence, altering side-chain types and their corresponding conformations. These changes can also have an indirect effect on the protonation states of nearby residues, influencing the enzyme's active site and overall structure. By generating a library of mutants, this stage allows us to explore the impact of specific changes on enzyme activity and stability, paving the way for more tailored enzyme designs.

Geometry variation is the third stage and involves modifications to the enzyme's conformation and the substrate reaction states. The efficiency of enzymatic catalysis is heavily influenced by the dynamic behavior of the

enzyme, which in turn is governed by how the enzyme conformation and substrate interactions evolve during the reaction. Protein dynamics, including conformational changes and flexibility, play a critical role in determining the enzyme's catalytic proficiency. By altering the geometry of the enzyme and its substrate complexes, this stage enables us to identify conformations that maximize the enzyme's reactivity and specificity toward the target substrate.

The final level, the energy engine, involves conducting computational energy calculations to assess the stability and catalytic potential of the designed mutants and their interaction with substrates. This step utilizes Molecular Mechanics (MM), Quantum Mechanics (QM), or a hybrid QM/MM approach to calculate the energy profiles of the enzyme-substrate complexes. These calculations allow us to evaluate key parameters such as binding affinity, transition state stabilization, and overall catalytic efficiency, providing crucial insights into the enzyme's performance. By assessing these energies, we can refine enzyme designs to enhance their activity and stability for specific applications.

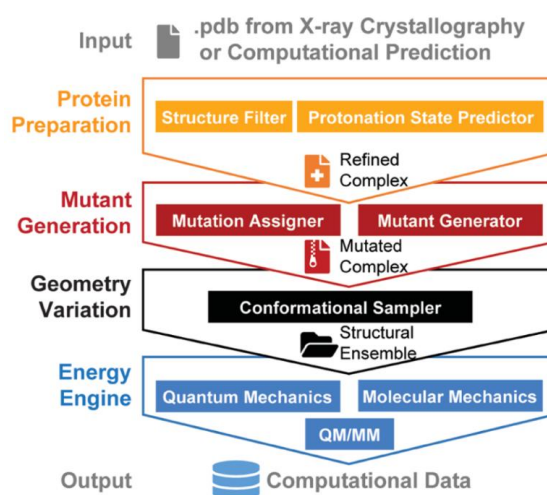


Figure S1: Hierarchical structure of high-throughput enzyme modeling. The framework involves four levels of operation, including protein preparation, mutant generation, geometry variation, and energy calculation. The framework takes in the enzyme structure as an input and delivers computational modeling data as an output.

Specifically, the workflow for enzyme design is organized into several modules, each handling a specific level of operations within the overall framework, including **protein preparation**, **mutant generation**, **geometric modifications**, and **energy calculations**. This modular design ensures a systematic and efficient approach to optimizing enzymes for various applications.

The first component of the workflow is the enzyme preparation module, which serves as the starting point by converting the initial enzyme structure into a computational model. This module generates the necessary standardized input files required for subsequent operations. It incorporates two primary functions:

Structural Filter: This function takes enzyme–complex structures as input and performs structural refinement. It removes unwanted components, such as missing loops, co-crystallization agents, and solvents, ensuring that only relevant structural data remain. It also retains chemically relevant ligands (such as inhibitors, substrates, intermediates, products, and structural analogs) that may be crucial for subsequent design steps. The structural filter ensures that the enzyme model is accurate and clean, ready for further processing.

Protonation State Predictor: This function predicts the protonation states of the enzyme's active site residues under physiological conditions, which is essential for understanding the enzyme's behavior during catalysis. Protonation states significantly impact enzyme function, especially in catalysis, where proton transfers are often involved.

In cases where no suitable enzyme–complex structure is available in public databases like the Protein Data Bank (PDB), users are required to manually curate the complex structure. This involves sourcing high-quality experimental data or constructing the complex through computational methods such as docking.

The protein preparation module is currently undergoing enhancements

aimed at improving its functionality and streamlining the enzyme design process. These updates include the development of a novel enzyme structure-repair function, which introduces three key capabilities:

This function automatically restores missing segments in the enzyme structure, addressing gaps that often arise in experimental structures. For cases where only substrate analogs are available, the module can convert these analogs into the corresponding active substrates, ensuring that the enzyme's interaction with the true substrate is accurately represented in the model. This feature allows for the creation of prereactive complexes by docking substrates into the enzyme's active site. This is crucial for simulating the enzyme-substrate binding events before the actual catalytic process begins.

These advancements will significantly enhance the flexibility and precision of the enzyme preparation module, making it capable of handling more complex structures and providing more accurate representations of enzyme–substrate interactions.

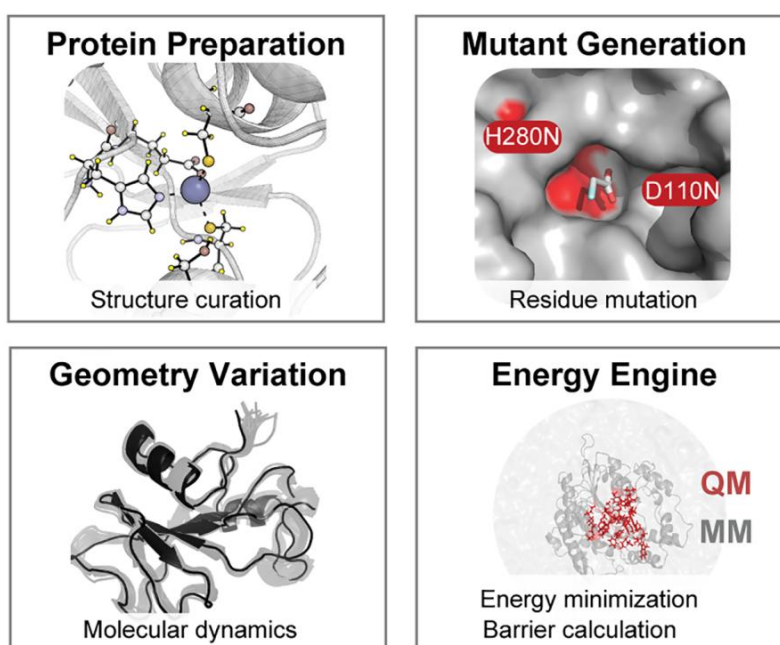


Figure S2: Four modules.

Origin of Prochiral Selectivity in PET- Hydrolyzing Enzymes

To delineate the mechanistic origin of prochiral selectivity in PET hydrolysis, we conducted a comparative analysis of structural geometry, electrostatic factors, and intrinsic electric fields along the full reaction coordinate for three benchmark enzymes: HiC, FAST-PETase, and LCC-ICCG. From a structural standpoint, we observed a conserved pattern of key geometric parameters—notably catalytic distances, nucleophilic attack angles, and dihedral orientations—across all systems during both substrate binding and transition-state formation (Figure S3). These conserved elements highlight the shared catalytic scaffold of cutinase-like enzymes.

However, pronounced local deviations were apparent between enzymes that correlate with differences in reaction energy barriers. Specifically, in the Re-face binding mode of HiC, the PET@C1–Ser@O1 and His@N1–Ser@H1 distances (3.5 ± 0.3 Å and 1.9 ± 0.1 Å, respectively) were substantially elongated compared to the tighter geometries found in FAST-PETase (2.5 ± 0.1 Å; 1.7 ± 0.0 Å) and LCC-ICCG (2.7 ± 0.2 Å; 1.7 ± 0.1 Å).

During the acylation step, HiC also displayed prolonged oxyanion-hole hydrogen bonds—notably PET@O4–Ser@H6 and PET@O4–Gln@H7—suggesting less efficient transition-state stabilization in comparison with FAST-PETase and LCC-ICCG.

Correlation Between Geometric Parameters and Reaction Energy Barriers
To further link structure to energetics, we performed linear regression analyses between geometric descriptors and computed reaction barriers. For FAST-PETase and LCC-ICCG, the PET@O2–His@N1 distance and the PET@O2–His@N1–Ser@H1 angle exhibited strong linear correlations with the barrier heights ($R^2 = 0.87$ and 0.90 for FAST-PETase; $R^2 = 0.92$ and 0.89 for LCC-ICCG, respectively; Figure S3b, c). These results identify elongated PET@O2–His@N1 distances and compressed PET@O2–His@N1–Ser@H1 angles as key determinants of increased reaction barriers and reduced prochiral selectivity in these two high-performance enzymes (Figure S3d).

In striking contrast, HiC displayed weak or negligible correlations for the same descriptors ($R^2 = 0.03$ and 0.36 , respectively), and inclusion of HiC in a combined analysis substantially lowered the overall coefficients of determination (e.g., from $0.76 \rightarrow 0.46$ for PET@O2–His@N1, and $0.65 \rightarrow 0.20$ for the PET@O2–His@N1–Ser@H1 angle).

The diminished predictive power of the canonical descriptors in HiC suggests a distinct structural bottleneck. Indeed, further analyses identified the PET@O4–Gln@H7 and PET@C1–Ser@O1 distances—proxies for oxyanion-hole stabilization and nucleophilic approach geometry—as the dominant determinants of prochiral selectivity in HiC. The weaker binding and diminished oxyanion-hole stabilization effectively elevate the reaction barrier for the Re-face pathway, leading to lower catalytic efficiency for this face (Figure S3e).

Collectively, these results underscore that while FAST-PETase and LCC-ICCG share a common geometric control mechanism—dominated by the His-assisted proton-shuttle geometry (PET@O2–His@N1) and its associated angle—HiC's prochiral selectivity originates primarily from suboptimal oxyanion-hole engagement and elongated nucleophilic distances. This mechanistic divergence highlights the importance of active-site preorganization and transition-state hydrogen-bonding networks in dictating facial selectivity and suggests that targeted engineering of oxyanion-hole residues could substantially improve HiC's catalytic profile.

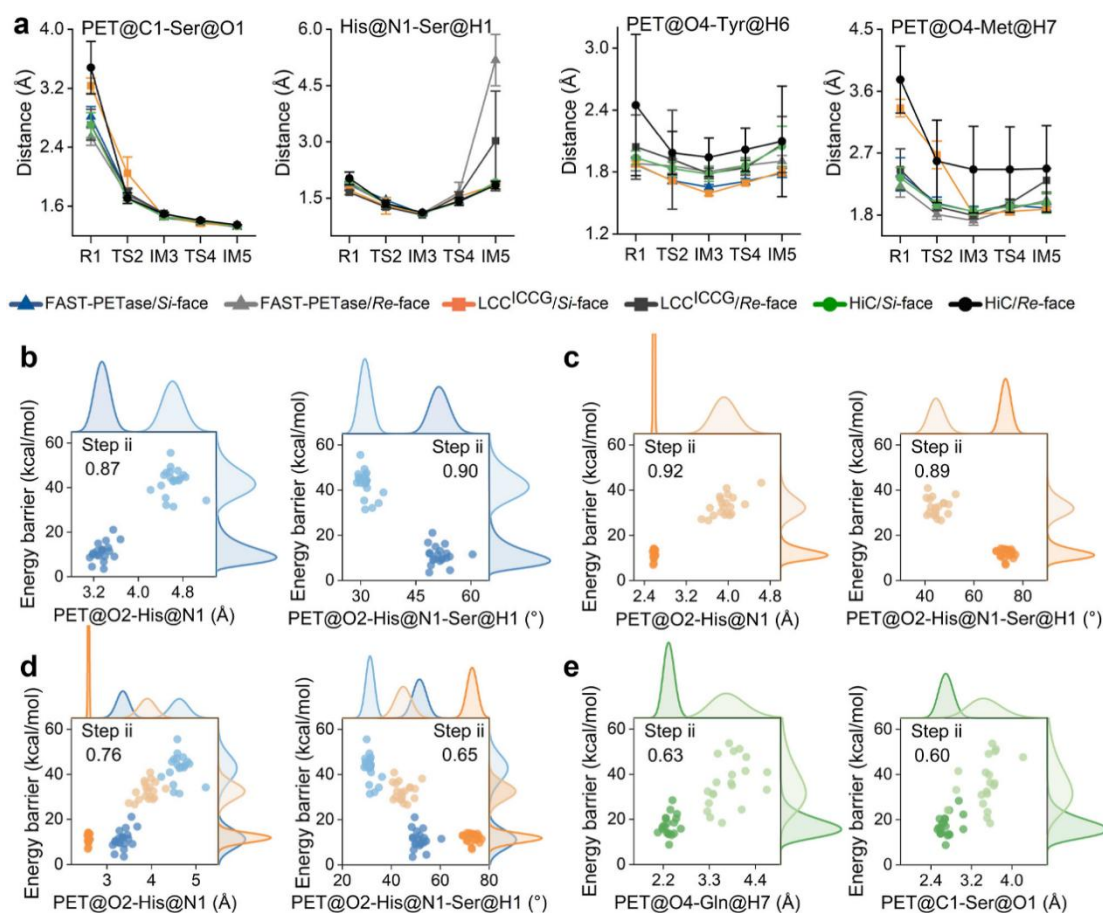


Figure S3: Influence of structure parameters on the selectivity. (a) Relevant structure variation along the reaction paths. (b–d) Correlation between distance of PET@O2-His@N1, angle of PET@O2-His@N1-Ser@H1, and energy barriers for FAST-PETase (b), LCC-ICCG (c), and two enzymes (FAST-PETase and LCC-ICCG together) (d), respectively. (e) Relationship between distances of PET@O4-Met@N4, PET@C1-Ser@O1, and energy barriers for HiC enzyme, respectively.

Directed Evolution and Activity Screening

The development of a high-throughput screening (HTS) workflow for evaluating PET-degrading enzymes hinges on four essential components:

Efficient Extracellular Enzyme Secretion: The enzyme must be secreted in high yields into the culture medium to avoid complex and time-consuming steps like cell lysis or protein purification.

Quantifiable PET Substrate: A PET substrate that is easily measurable in assays ensures that enzyme activity can be directly correlated with PET degradation.

Sensitive Enzymatic Activity

Assay: A rapid, reliable, and sensitive assay is needed to evaluate enzymatic efficiency and selectivity. **Interference-Free Culture Medium:** The culture medium should not introduce any background signals that could interfere with the assay's ability to accurately measure enzyme activity.

For the *Escherichia coli* BL21 (DE3) host system, one major challenge lies in the low secretion levels of extracellular proteins, while these cells are known to accumulate a high level of intracellular proteins. Given this, the direct use of culture supernatants from *E. coli*, in the absence of extensive purification, could significantly simplify the workflow and enhance throughput if ICCG (the PET-degrading enzyme) can be efficiently secreted.

Our goal was to engineer ICCG expression vectors that would enable efficient secretion of the enzyme into the extracellular environment. This would potentially allow the culture supernatant to be used directly in activity assays, eliminating the need for the otherwise essential step of cell disruption or protein purification.

Signal Peptide Variants for ICCG Secretion

To facilitate extracellular secretion, four signal peptides were tested by fusing them to the N-terminus of ICCG. SPzof: A highly efficient secretion signal peptide, previously screened in our laboratory for optimal extracellular expression. SPpee: A Sec-dependent translocation signal peptide known for its robust secretion capabilities. SPpeB.G58A: A variant of the *pelB* signal peptide with a mutation at G58A, designed to improve secretion efficiency. SPu: The maltoporin signal peptide, typically used for periplasmic secretion. Additionally, to explore the possibility of signal-peptide-free secretion, an expression vector was constructed where ICCG was expressed without any signal peptide, based on previous reports that certain proteases (such as keratinases) can be secreted extracellularly without the need for a signal peptide. The constructed vectors were transformed into *E. coli* BL21 (DE3), with the empty vector serving as a control. The resulting cultures were then subjected to SDS-PAGE analysis to assess both intracellular and extracellular protein levels. This analysis allowed for a direct comparison of the secretion efficiencies of each ICCG variant.

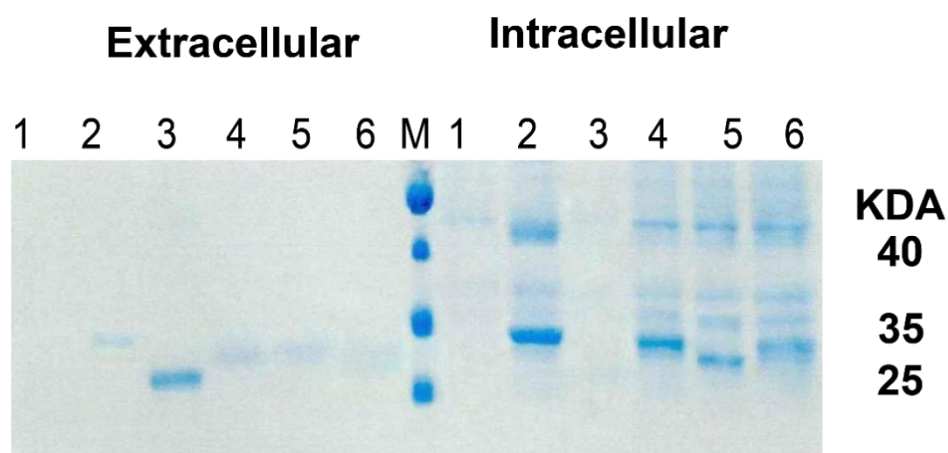


Figure S4: SDS-PAGE analysis of ICCG secretion. Extracellular, culture supernatant; M, molecular mass standard protein; Intracellular, cell lysate; I, *E. coli* BL21 (DE3); 2, SPN2.-ICCG; 3, ICCG without signal peptide.

Expression and purification of ICCG mutants

The mutant plasmid was transformed into an *E. coli* expression strain and induced with 0.6 mM IPTG at 16°C for 18 hours to express the mutant protein. Using the AKTA Pure automated purification system, the mutant protein was purified by two nickel affinity chromatography cycles. The purified protein was analyzed by SDS-PAGE (the red portion indicates the target protein).

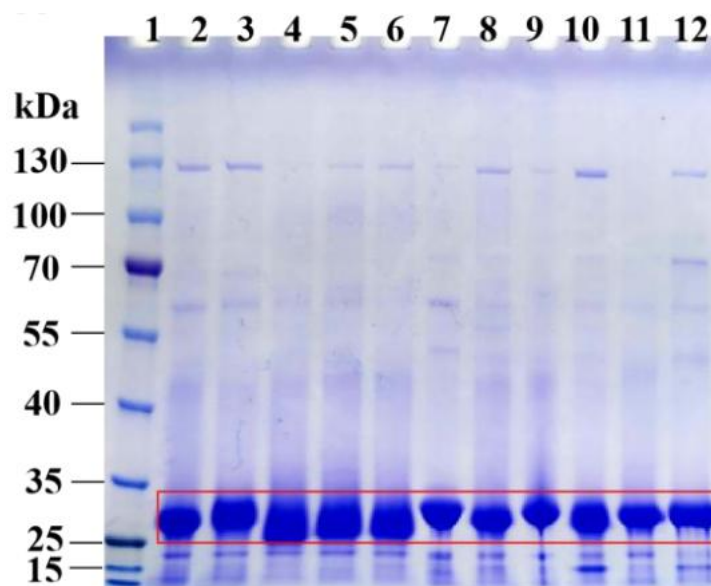


Figure S5: A 1: Marker; 2: ICCG; 3: H218Y; 4: T211N; 5: H218F; 6: A97D; 7: T211Q; 8: H218W; 9: T211A; 10: T211F; 11: H218L; 12: T211S.

Prior to conducting enzyme activity assays, the mutant protein samples were first quantified using the Thermo Protein Quantification Kit to ensure consistent protein concentration across all experimental groups. This step is critical, as uniform protein loading minimizes variability in subsequent activity measurements. ICCG (Isolated Cutinase from *Geobacillus stearothermophilus*) exhibits inherent thermal stability, with optimal activity at 72°C; however, to screen for thermostable mutants, we aimed to evaluate performance under elevated temperatures. Thus, enzyme activity was assessed at three distinct temperatures: 70°C, 80°C, and 90°C, using amorphous PET film as the substrate. Reactions were incubated for 24 hours under these conditions to allow sufficient substrate conversion. Post-incubation, enzymes were inactivated by heating samples to 100°C for 15 minutes to halt catalysis. The mixture was then centrifuged at 11000 rpm for 10 minutes to pellet insoluble debris, and the supernatant containing soluble degradation products was collected for further analysis.

The degradation products of PET, terephthalic acid (TPA) and mono(2-hydroxyethyl) terephthalate (MHET), possess aromatic rings that confer UV absorbance, enabling their detection via high-performance liquid chromatography (HPLC). HPLC analysis was performed at a wavelength of 254 nm to quantify these products. A mobile phase consisting of KH_2PO_4 (pH 2.5) and methanol was employed with linear gradient elution to separate TPA and MHET. Chromatographic separation revealed distinct retention times: TPA eluted at 8.6 minutes, while MHET eluted at 9.2 minutes, indicating that TPA exhibits stronger polarity than MHET (as shorter retention times on a reverse-phase column typically correlate with higher polarity).

To correlate UV peak areas with product concentrations, standard curves were generated using purified TPA and MHET standards. By plotting the UV absorbance peak areas against known concentrations of these standards, linear regression models were established. These standard curves were then used to calculate the concentrations of TPA and MHET in the experimental samples, providing a quantitative measure of ICCG mutant enzyme activity at each tested temperature. Together, these steps enable systematic evaluation of thermostability and catalytic efficiency among ICCG variants.

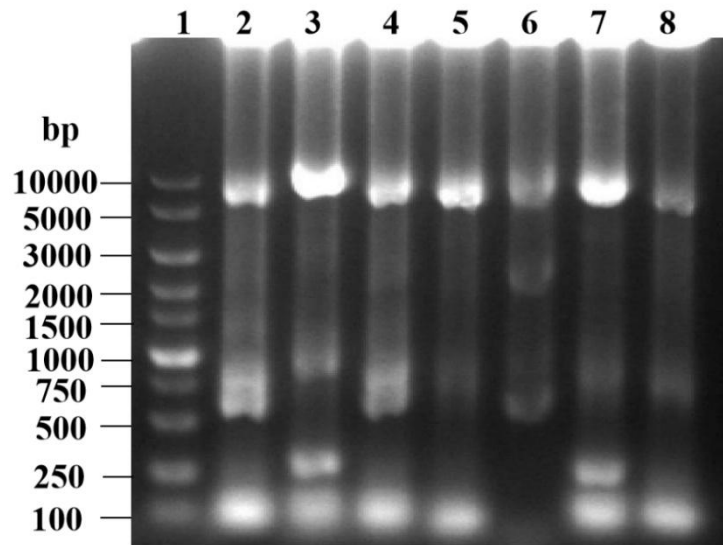


Figure: The PCR product of triple mutation.

Ni-affinity chromatography (primary & secondary purification)

Purification leveraged the specific binding of the His-tag on the target protein to nickel (Ni^{2+}) ions immobilized on a resin, with imidazole acting as a competitive eluent to separate the protein from contaminants. First, the clarified lysate was filtered through a 0.22 μm membrane to eliminate particulates that could foul the column. The filtrate was loaded onto an AKTA Pure automated system equipped with a Ni-NTA affinity column equilibrated with 1 \times Ni Buffer A (20 mM imidazole, 50 mM Tris-HCl pH 8.0, 300 mM NaCl). A linear gradient elution was performed over 80 minutes, increasing imidazole concentration from 20 mM to 300 mM (1 \times Ni Buffer B) to elute bound proteins. This gradient removed >80% of non-specifically bound impurities, while the triple mutant—fused to a TrxA tag for solubility—eluted as a distinct peak monitored by UV absorbance at 280 nm. Fractions corresponding to this peak were pooled for downstream analysis.

Verification of Purified Protein by SDS-PAGE

To confirm the purity and molecular weight of the eluted protein, SDS-PAGE was conducted. Purified fractions were mixed 4:1 with 5 \times loading buffer (containing SDS, β -mercaptoethanol, and bromophenol blue) and heated at 95°C for 10 minutes to denature proteins. Samples were loaded onto a 12% polyacrylamide gel and separated by electrophoresis alongside a

molecular weight marker. Post-staining with Coomassie Brilliant Blue R-250, a single intense band was observed at ~47 kDa—consistent with the expected size of the TrxA-fused triple mutant (TrxA: ~12 kDa; triple mutant: ~35 kDa). This result validated successful purification of the target protein with high purity (>95%, as estimated by densitometry), ready for subsequent functional assays.

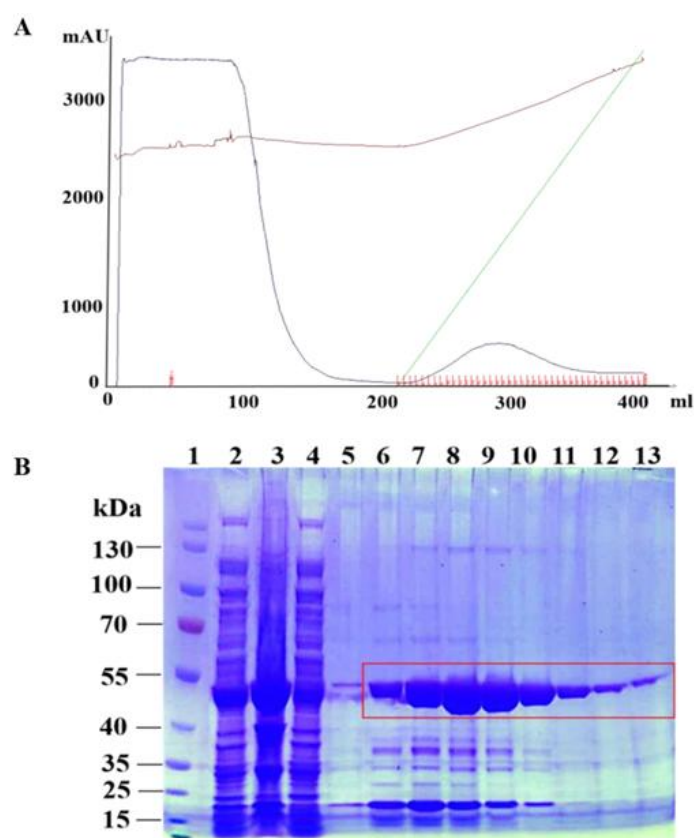


Figure: Nickel column affinity chromatography and SDS-PAGE analysis of H218Y/N248D/S247A. A: Nickel column affinity chromatography of H218Y/N248D/S247A; B: SDS-PAGE analysis. 1: Marker; 2: Supernatant after lysis; 3: Centrifugation precipitate after lysis; 4: Sample wash flow-through; 5-13: Elution collection solution; (Note: Red boxes indicate target bands).

Before enzyme activity testing, ICCG and its mutants were quantified using a protein quantification kit coupled with a microplate reader. The triple mutant enzyme activity was tested using PET as the substrate, with reactions at 70°C, 80°C, and 90°C for 24 h. After the completion of the enzyme activity test, several mutants were observed to have a significant hydrolysis effect on PET. The observed phenomena were photographed and revealed that at 70°C,

ICCG and the mutants completely degraded PET (Figure A), while PET flakes remained at 72°C and 75°C. At 72°C, all enzyme reactions showed no significant change compared to the control (Figure B). However, at 75°C, an interesting phenomenon was observed: PET fragments were degraded in the triple mutants, with KRP showing the highest concentration of small PET fragments, while no similar phenomenon was observed in ICCG (Figure C). This observation suggests that the modified triple mutant H218Y/N248D/S247A exhibited higher hydrolysis efficiency than ICCG at 75°C.

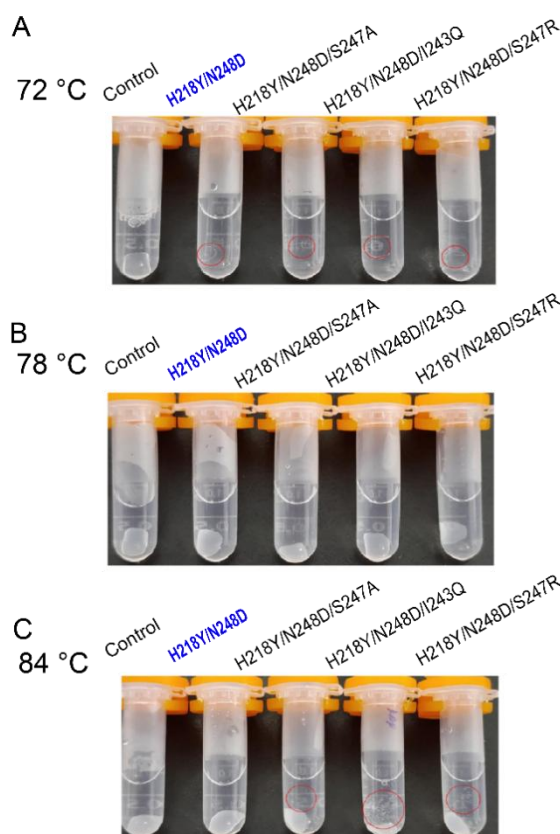


Figure: A, B, and C represent the degradation of PET by the triple mutants at 72°C, 78°C, and 84°C, respectively, after 24 h of reaction.

PETase engages PET oligomers through four subsites (I–IV), enabling productive binding of a tetrameric model substrate (4PET). By analogy, structural analysis of the LCC-ICCG scaffold indicates a comparable overall substrate-binding architecture. Notably, however, the ICCG surface displays a constricted conduit framed primarily by residues S247 and I243 that partitions the binding surface into two PET-interacting regions. In this “two-region” topology, region 1 is contiguous with the catalytic cleft, whereas region 2 is

partially sequestered behind the S247–I243 bottleneck.

Rigid-receptor docking with PET oligomers is consistent with this anatomy. Region 1 readily accommodates a trimeric oligomer (3PET), providing shape complementarity along the cleft and stabilizing interactions with the terephthalate repeat units. In contrast, the narrow S247–I243 isthmus limits threading of the polymer chain toward region 2, thereby disfavoring poses in which longer oligomers span both regions. As a result, the wild-type ICCG channel is predicted to be suboptimal for binding 4PET (and longer PET segments) in an extended conformation that simultaneously occupies regions 1 and 2.

Structure-guided substitutions that soften or reorient the bottleneck markedly alter this landscape. Introducing N248D, S247A, and I243Q widens the inter-region passage and reduces steric and desolvation penalties for chain translocation. Quantitatively, the minimum channel width increases from 5.9 Å in LCC-ICCG to 8.9 Å and 9.6 Å in LCC-ICCG-R2 and LCC-ICCG-R3, respectively. In silico, these engineered channels permit 4PET to traverse the conduit and establish contacts within region 2 for both R2 and R3 variants, yielding low-strain poses that bridge the two regions.

Taken together, these data support a mechanistic model in which channel widening enhances substrate adaptability of LCC variants by (i) enabling longer PET chains to adopt extended, multi-subsite binding modes and (ii) permitting more extensive π – π and van der Waals contacts along the walls of region 2. The current structure-and-docking results already provide a coherent rationale: relieving the S247–I243 constriction enables productive occupancy of PET-binding region 2 by longer oligomers, thereby strengthening specific enzyme–substrate interactions and improving apparent binding affinity.

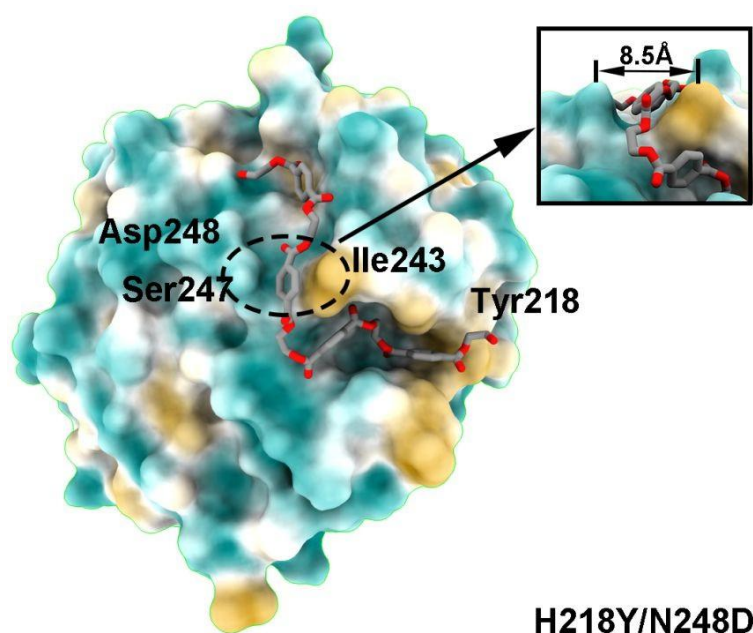


Figure: Structural features of the LCC variant LCC-ICCG-R2. Molecular docking of LCC-ICCG-R2 (ICCG^{H218Y/N248D}) with 4PET. Compared to the 5.9Å channel diameter between S247 and I243 in ICCG, after mutation, the channel diameter reached 8.5Å.

Poly(ethylene terephthalate) (PET) is known to undergo rapid recrystallization at temperatures above ca. 72 °C, which severely diminishes its enzymatic depolymerization efficiency by reducing polymer chain mobility and accessibility at the crystalline–amorphous interface. Conventional extrusion-based pretreatment—often employed to reduce the particle size of PET feedstock—has been reported to decrease the polymer’s molecular weight because of thermal–mechanical degradation during processing. However, low-molecular-weight PET chains are more prone to chain reorganization and recrystallization under elevated temperatures, thus presenting an unfavorable substrate state for enzymatic hydrolysis.

To mitigate these detrimental effects, we adopted a furnace-melting pretreatment protocol designed to maintain the intrinsic molecular weight and structural stability of the PET feedstock. The structural integrity and crystallization resistance of the furnace-pretreated PET proved crucial for

biocatalytic processing. The LCC-ICCG-R2 variant, operating at 78 °C, exhibited efficient depolymerization of the furnace-pretreated PET substrate, underscoring the beneficial synergy between substrate thermal stability and enzyme thermostability. By mitigating heat-induced recrystallization, the furnace-melting approach delivers a PET substrate that is more consistently hydrolysable under high-temperature reaction conditions.

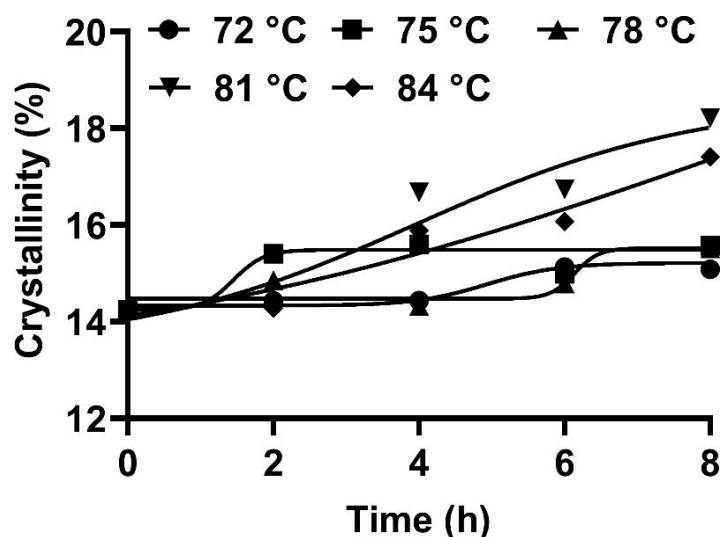


Figure: Crystallinity kinetics of Pc-PET at 72 °C, 75 °C, 78 °C, 81 °C and 84 °C. The crystallization kinetics curve was fitted using the sigmoid function.

The structural integrity and crystallization resistance of the furnace-pretreated PET substrate were pivotal for its successful biocatalytic processing. The LCC-ICCG-R2 variant, operating at 78 °C, demonstrated efficient depolymerization of the furnace-pretreated PET, highlighting the beneficial synergy between the thermal stability of the substrate and the thermostability of the enzyme. By effectively mitigating heat-induced recrystallization, the furnace-melting pretreatment provides a more stable and consistently hydrolyzable PET substrate under high-temperature reaction conditions, thus enhancing the overall efficiency of the enzymatic depolymerization process.

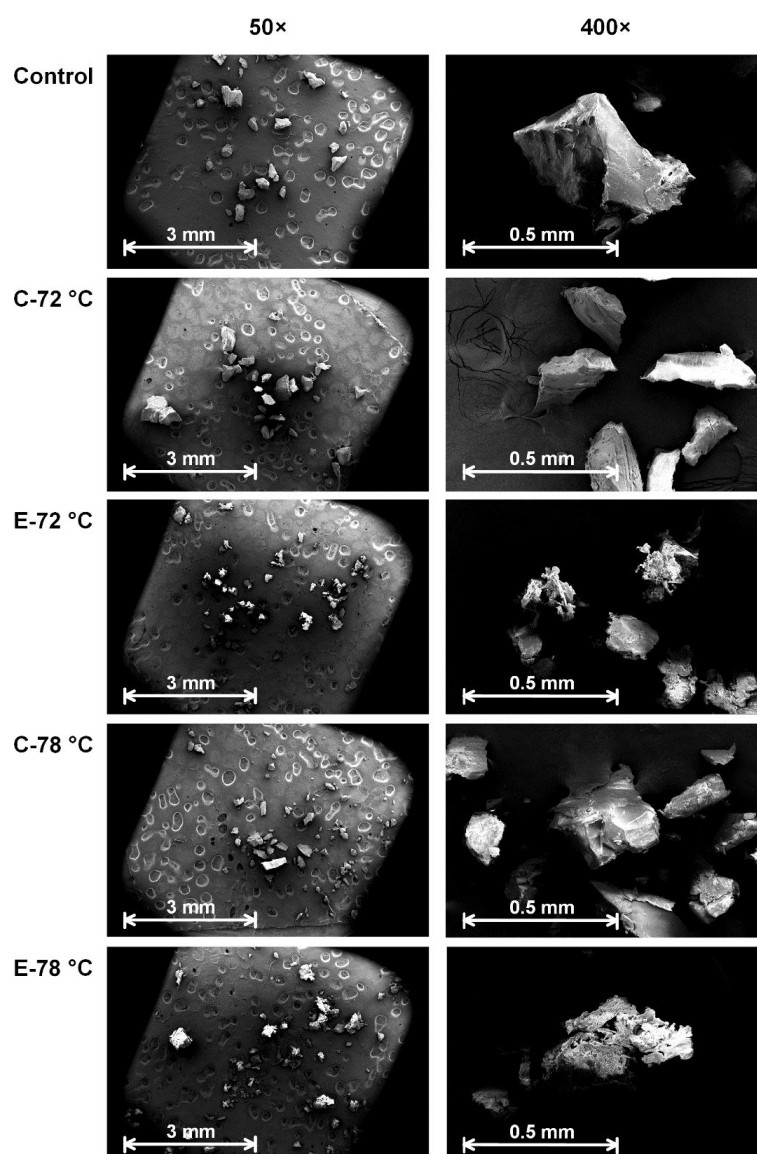


Figure: The morphological changes of PET powders observed by scanning electron microscopy. C-72 °C and C-78 °C indicate without the addition of PET hydrolase. E-72 °C and E-78 °C indicate adding LCC-ICCG-R2. 50 × and 400 × indicate the folds of magnification.

To further improve the depolymerization efficiency, we investigated the biodepolymerization of PET by the optimal variant LCC-ICCG-R2 at higher temperatures. The results showed that as the reaction temperature increased from 72°C to 78°C, the PET depolymerization rate continued to increase, while the catalytic rate began to decrease as the temperature continued to rise.

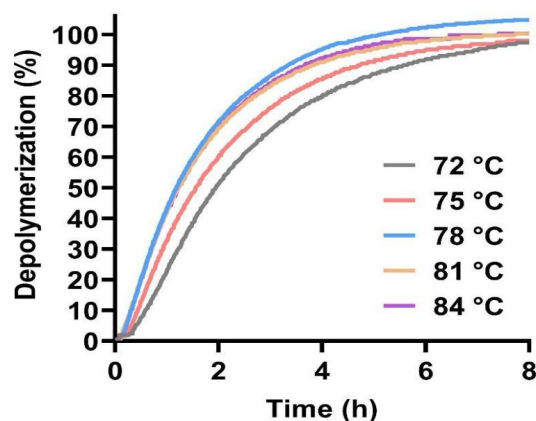


Figure: Bio-depolymerization of post-consumer PET bottles by LCC-ICCG-R2 at different temperatures. Comparison of the Pc-PET depolymerization kinetics of LCC-ICCG-R2 using 200 g kg^{-1} pretreated PET and 0.6 g kg^{-1} enzyme. The depolymerization process was carried out in 0.1 M phosphate buffer (pH 8.5) at different temperatures. The pH was maintained by titrating aqueous NaOH to neutralize the acidic product TPA produced by the PET depolymerization. The percentage of PET depolymerization was calculated based on the consumption of NaOH.

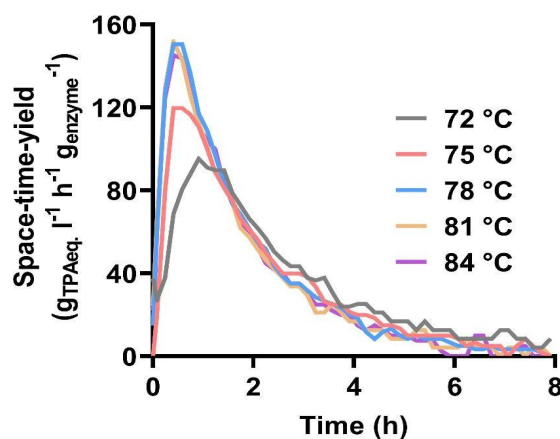


Figure: The specific space-time-yield product of LCC-ICCG-R2 in different temperatures. Comparison of the specific space-time-yield product from LCC-ICCG-R2. The equivalent TPA quantity (TPAeq.) was converted from the consumption of NaOH.

Table: The first round of variants predicted by MD simulation of binding free energy and their relative activity assessed by A₂₄₀.

Variant	Affinity energy	Relative activity
M166A	-7.08	0.014
A97N	-6.66	0.000
T211A	-6.54	1.008
T211S	-6.46	0.889
H218F	-5.86	1.096
T211N	-6.2	1.102
A97K	-6.16	0.117
H218L	-6.12	0.896
ICCG	-5.32	1.000
A97D	-5.92	1.081
T211Q	-5.9	1.063
T96Y	-5.9	0.450

Synthesis and Degradation of Novel Biodegradable Polyesters

PBTDP: Hydrophilicity-Enhanced Copolyesters

Conventional PE-like polyesters (e.g., PE-18,18) exhibit extremely slow degradation in natural environments, with a weight loss of <0.2% after 50 days. Their recycling requires industrial composting conditions (60°C) or strong chemical reagents (e.g., methanol), which hinders the realization of a green closed-loop cycle. In this study, bio-based pyrrolidone dicarboxylic acid (EBPCA) was synthesized via polycondensation of bio-based ethylenediamine and itaconic acid, and then incorporated as a comonomer into the polyester backbone to prepare the PBTDP series of polyesters (where x denotes the molar percentage of EBPCA). The pyrrolidone ring endows the material with dual functions: (1) acting as hydrophilic sites to enhance surface hydrophilicity; (2) serving as enzyme-binding sites to strengthen non-covalent interactions with lipase CALB. Performance tests revealed that when the EBPCA content was increased to 25 mol% (PBTDP25), the weight loss reached nearly 40% after 50 days of incubation in 37°C water, significantly outperforming the conventional PE-like polyester (PBTDP0, with a weight loss of <2%). Furthermore, enzymatic degradation efficiency under CALB catalysis was remarkably improved: PBTDP25 completely fragmented within 10 days, and the degradation rate increased positively with the EBPCA content.

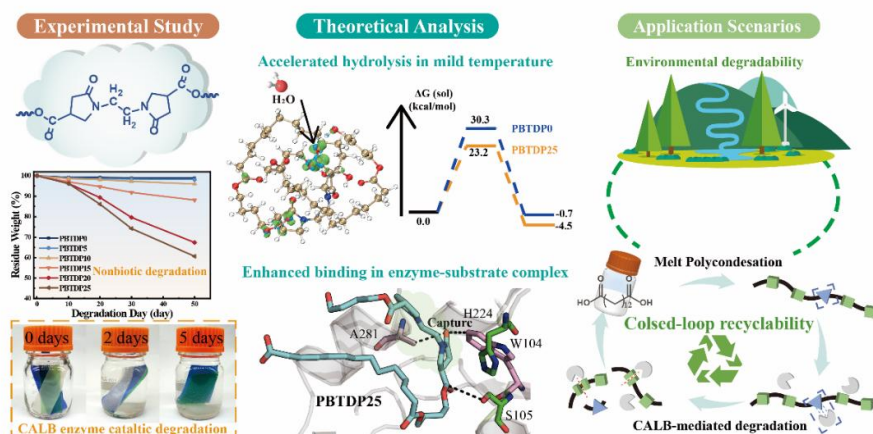
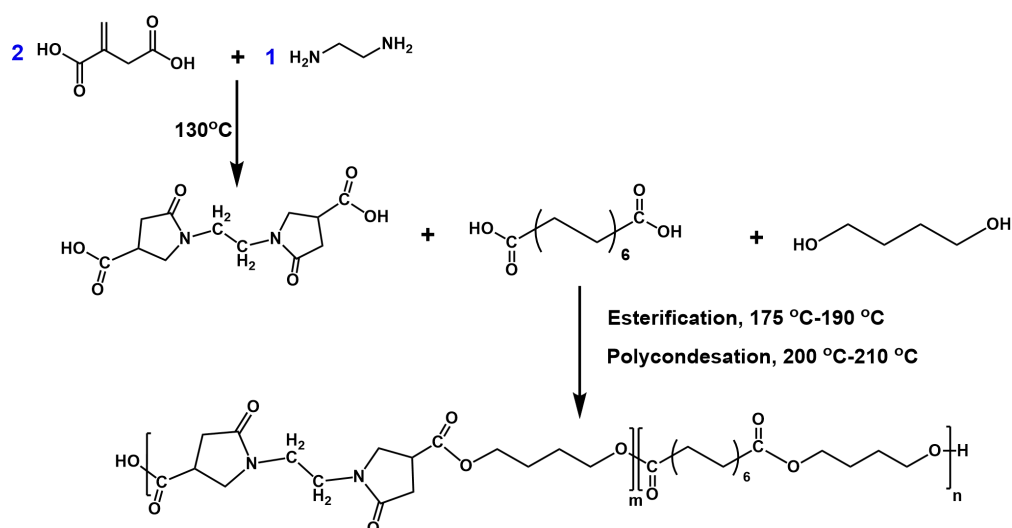


Figure: Future research will be dedicated to facilitating more efficient and large-scale application of enzymatic recycling design based on immobilized enzyme technology to reduce the production inputs of a biocatalyst and make greater contributions to the greening of polymer enzymatic recycling.

Synthesis of EBPCA monomer

IA (0.6 mol) and EDA (0.3 mol) were dissolved in 500 mL of water in 1000 mL three-necked round-bottom flasks equipped with a mechanical stirring. The reaction mixture was stirred at reflux (130 °C) for 36h. The formed solution was subjected to reduced pressure to remove the water. Secondly, the products were precipitated, followed by filtration and washed with cold methanol, and drying in vacuo overnight at 50 °C.

Synthesis procedure



Scheme: Synthesis of EBPCA monomer and PBTDP copolyesters.

Utilizing feedstocks derived from biomass to manufacture valuable polymers is an attractive approach. Firstly, the renewable pyrrolidone diacid EBPCA was successfully synthesized from bio-based ethylenediamine and itaconic acid,^{35–38} as confirmed by ¹H NMR and FT-IR spectra.

Characterization data for EBPCA monomer

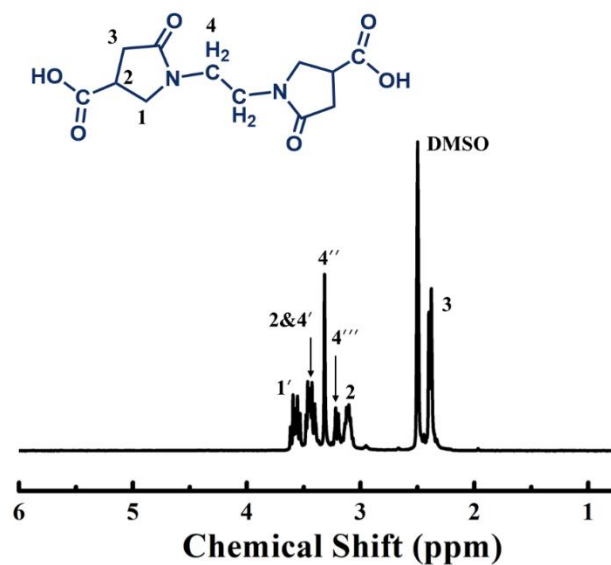


Figure: ¹H NMR (400 MHz, DMSO) of EBPCA monomer: 3.62-3.52 (2 H, m), 3.49 -3.42 (2 H, m), 3.40 (1 H, s), 3.32 (2 H, s), 3.21 (1 H, d), 3.10 (2 H, m), 2.40 (4 H, t).

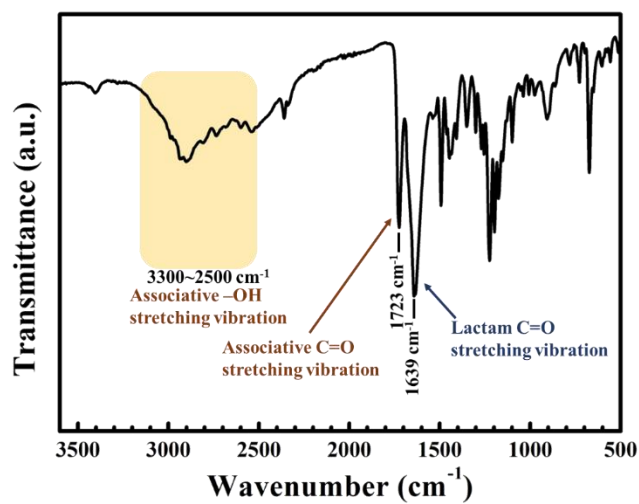


Figure: FT-IR spectra of EBPCA monomer powder.

^{13}C NMR provided more detailed structural information on PBTDPs, as shown in Fig. 2c and d. Peaks of A and B (173–174 ppm) were assigned to the carbonyl groups of ester bonds, and peak C at 172 ppm corresponded to the carbonyl groups of the lactam ring. Besides, peaks of E, F and I were attributed to the $-\text{CH}_2-$ of the pyrrolidone ring, respectively. Moreover, the chemical shifts of protons H and J in methylene of the long-chain diacid appeared at 46 and 25 ppm. Specifically, the signal peaks of proton K were provided by methylene groups in multiple chemical environments, and more detailed analysis is provided.

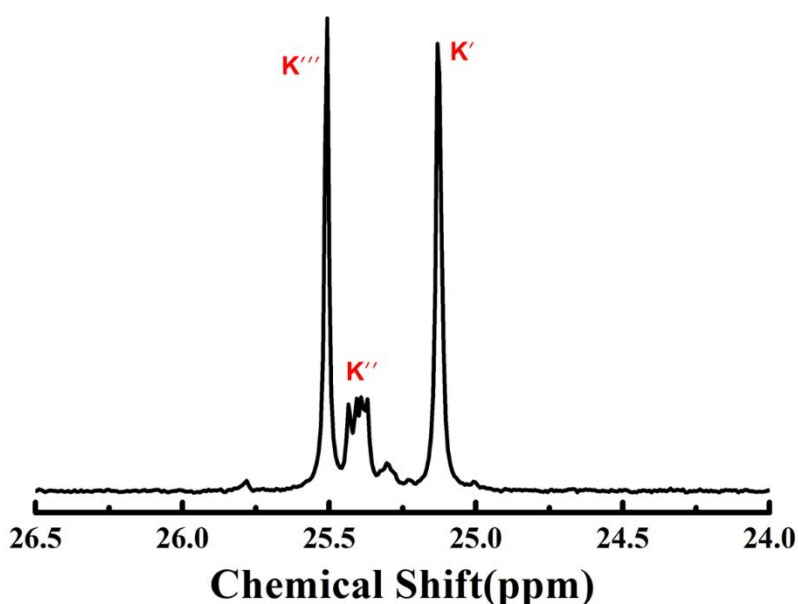


Figure: ^{13}C NMR spectra with enlargement of the region between 26.5 and 24.0 ppm.

Enzymatic recycling of PBTDPs from mixture plastics. The degraded products after enzymatic degradation can serve as building blocks for recycling, which represents an environmentally friendly strategy for enhancing the potential for the reuse of polymers within a circular economy. The enzymatic recycling and separation of targeted materials from mixed plastic

waste streams is a key point toward sustainability. Thus, the depolymerization of PBTDP20 and monomer recovery from mixed plastic waste are shown. Pieces from various plastics, such as PP (blue), PVC (green) and PET (transparent), were mixed with PBTDP20. The polymer mixture was exposed to the same enzymatic solution. Because of the orthogonal reactivity and the chemical stability of the other plastic products under the given conditions, PBTDP20 was selectively depolymerized. Within 2 days, the bulk material started to break and the formed TDA precipitated as a fine powder, while pyrrolidone oligomers remained dissolved in the aqueous mixture. As a result, the TDA monomers with a recycling rate of 92% could be easily separated from the mixed.

Similar to the hydrolysis process, PBTDP15, PBTDP20 and PBTDP25 degraded faster than PBTDPs with a lower ratio of pyrrolidone under enzymatic conditions, due to the improved hydrophilicity and reduced crystallinity of copolyesters themselves. Surprisingly, PBTDP20 and PBTDP25 were completely shattered after 10 days, while other specimens retained their entire frames.

Hydrolysis Behavior of PBTDPs

The hydrolysis experiment of PBTDPs was conducted in PBS solution at 37 °C by using hot-pressed dumb-bell specimens. PBTDP0 was observed virtually no mass loss (<2%) after hydrolysis for 50 days. PBTDP5 and PBTDP10 also showed high residue weights over 96%, respectively. As reported elsewhere, PE-like polyesters were usually difficult to hydrolyze directly in mild temperature due to the hydrophobicity of the methylene backbone and high crystallinity of polyesters. With the increase of BP units, the residue weight of PBTDPs continuously reduced, and PBTDP25 displayed the fastest hydrolysis rate, with 60.6% of the residue weight. The surface morphologies of samples after hydrolysis were studied using SEM. PBTDP0 and PBTDP5 maintained a flat morphology, as well as minimal corrosion

appeared on the surface of the PBTDP10 after 50 days of hydrolysis. The images of PBTDP15 showed more cracks, which facilitated further surface degradation. Full planes were almost non-existent in PBTDP20 and PBTDP25, and the surface became irregular and more pores appeared. The change in molecular weight also demonstrated that the introduction of pyrrolidone as a hydrophilic group into the molecular chain could significantly improve the hydrolysis degradation.

The above results illustrated that the pyrrolidone units were the most critical factor affecting the hydrolysis of polyesters. To further understand the hydrolytic pathways, the PBTDP0 and PBTDP25 were selected to perform theoretical calculations based on Fukui function analysis and DFT calculation. Specifically, the Fukui function analysis based on the low-energy conformers was conducted to illustrate the reactivity trends and site selectivity. Fukui indices (f^+) represented the reducibility of carbonyl carbon according to nucleophilic attack ability. As a result, the ester bonds adjunct to the pyrrolidone functional groups (f^+ index of C1: 0.0843) were most reactive for nucleophilic attack among carbonyl carbons of PBTDP25 segment. In contrast, the f^+ of PBTDP0 carbonyl carbons was low (0.0256), indicating their lower reactivity. The hydrolysis reaction of PBTDP25 was further studied via the final optimized geometries and the transition state structure was exhibited. The Gibbs activation energy of PBTDP25's hydrolysis process was calculated to be 23.2 kcal/mol, which is 7.1 kcal/mol lower than that of PBTDP0. The hydrolysis transition states of esters in PBTDP25 were calculated and shown in Figure 5e. To unravel the origin of preferable energy barrier of PBTDP25, the independent gradient model based on Hirshfeld partition (IGMH) was used to visualize and quantify the noncovalent interactions between PBTDP25 and water molecules. As a result, PBTDP25 processed the vast blue area, responding to the typical hydrogen bond (Figure f).

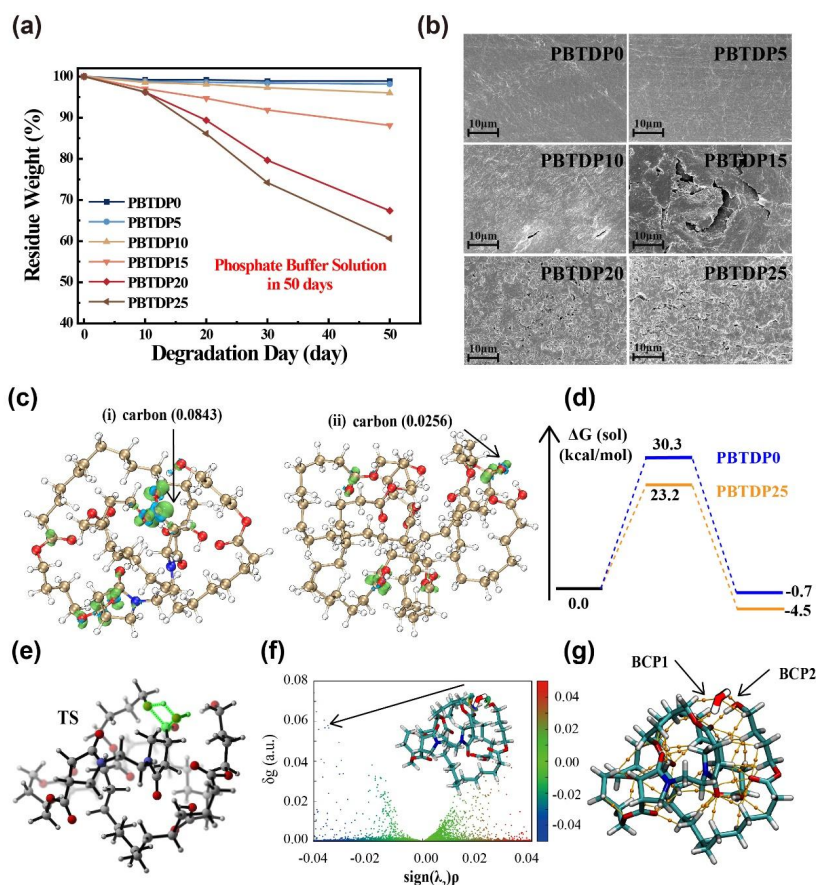


Figure: (a) Residue weights of PBTDPs degraded in PBS solutions during 50 days. (b) SEM photos of the surface morphologies of PBTDPs at 3500 \times after 50 days of hydrolysis in PBS solutions. (c) Hydrolytic pathways were calculated with the DFT method. Fukui function analysis results of (i) PBTD25 and (ii) PBTD0 with an isosurface value of ± 0.005 (blue, negative; green, positive). (d) Free energy profile for hydrolytic mechanism. The relative free energy profiles calculated with ω B97X-D/6-31+G(d,p) level of theory. Energies are in kcal/mol. (e) The transition state structure of PBTD25. (f) Interaction analysis between PBTD25 and water molecules. Blue isosurface represents the hydrogen bonding attraction. (g) Hydrogen bond strength identification via QTAIM analysis. The water molecules are highlighted. Bond critical points are shown in small orange spheres.

The hydrolysis of polyesters is a process whereby ester bonds are broken down by water molecules, which is dependent on a number of factors, including the hydrophilicity, crystallinity and chemical structures of the polyester. Obviously, the results of accelerated weight loss and broken surfaces were closely related to the ratio of pyrrolidone units. The declined water contact angles (WCA) showed that the polarity of pyrrolidone units enhanced the affinity of polyester with water. Besides, pyrrolidone units also slightly disrupted the crystallization of the material, resulting in the exposure of more amorphous areas that were susceptible to attack by water molecules.

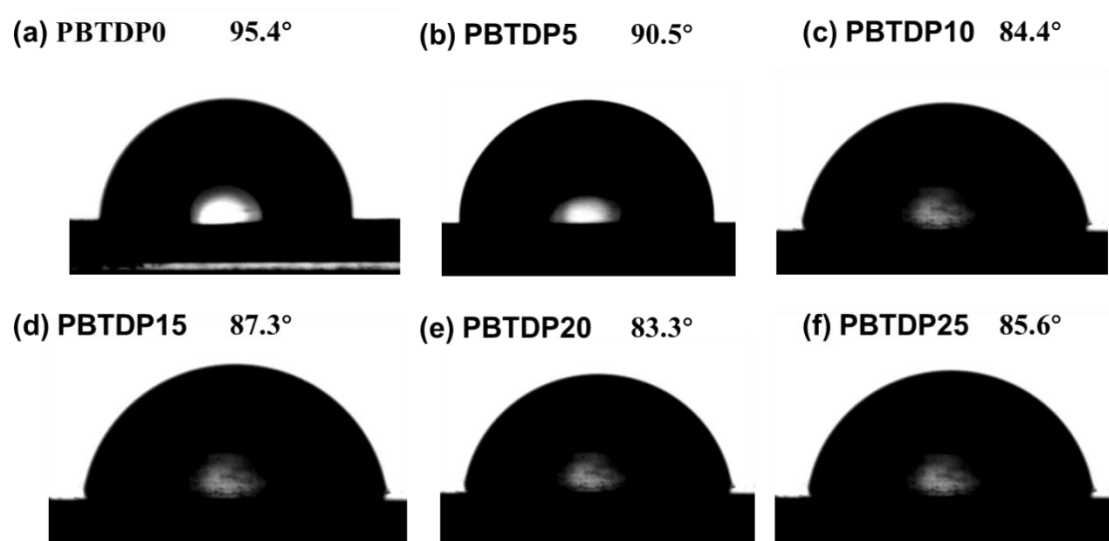


Figure: The water contact angle plots for (a) PBTDP0, (b) PBTDP5, (c) PBTDP10, (d) PBTDP15, (e) PBTDP20 and (f) PBTDP25.

To further explore the hydrolysis mechanism, the ATR-FTIR and ^1H NMR were employed to analyze the residues of PBTDPs after hydrolysis. After hydrolysis, more obvious terminal $-\text{OH}$ or $-\text{COOH}$ absorption peaks at 3300 – 3700 cm^{-1} and the newly generated carbonyl stretching vibration peak was located at 1658 cm^{-1} appeared, indicating the breakage of esters bonds. The specific change of components was calculated based on signal peaks of *a* and *b* in ^1H NMR spectra. Compared with the original samples, the residual composition of pyrrolidone segments was less than that of long-chain diacids,

suggesting that the ester bonds of the pyrrolidone segments were preferentially degraded in the aqueous environment.

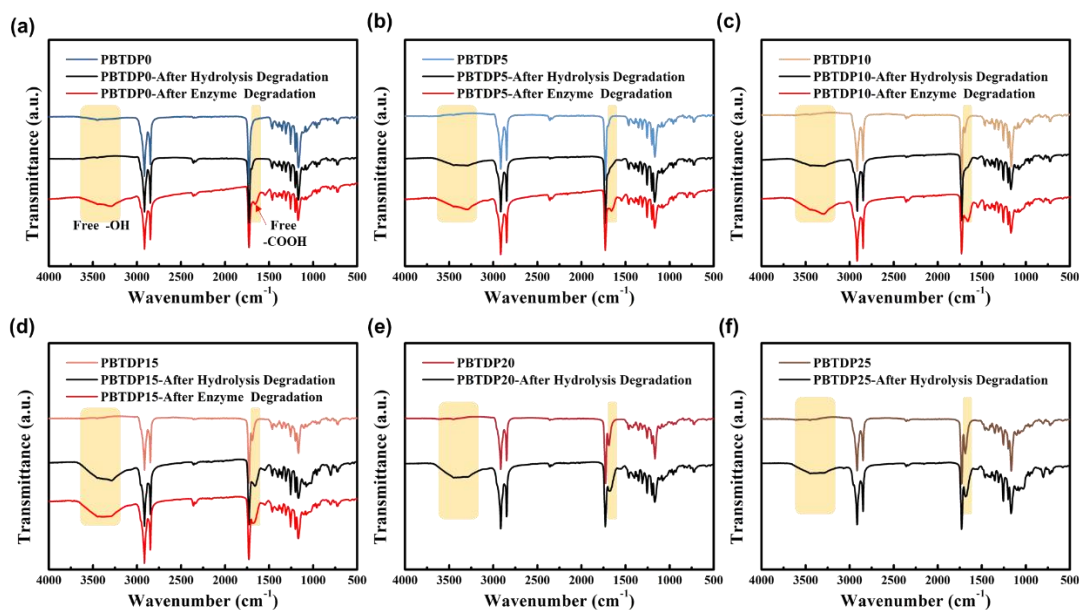


Figure: Changes in the ATR-FTIR spectra of PBTDPs after degradation experiments.

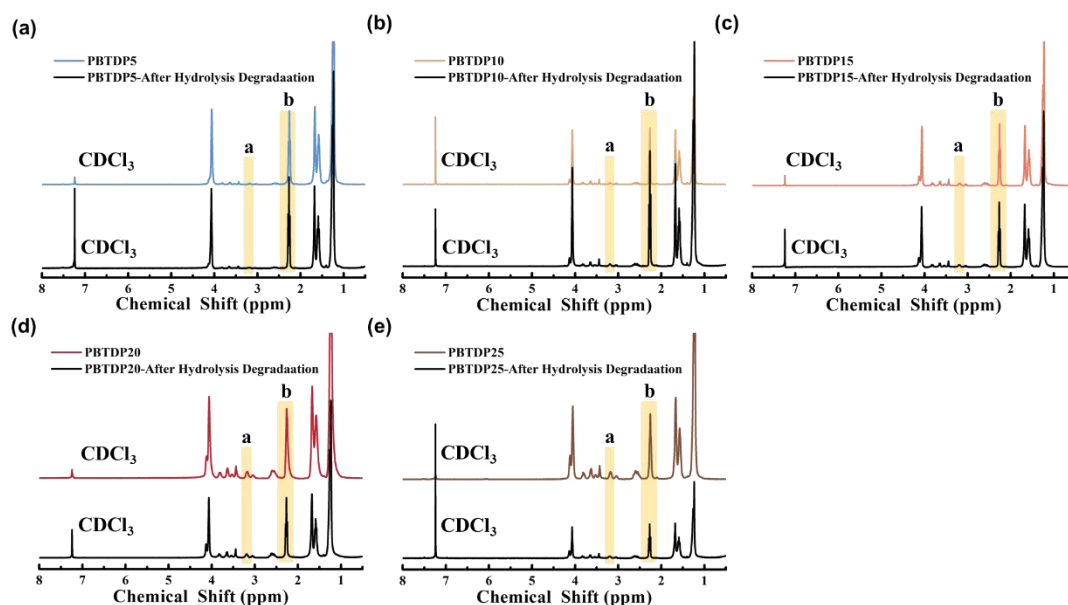


Figure: Changes in molecular structure of PBTDPs before and after hydrolysis experiment.

Similar to the hydrolysis process, PBTDP15, PBTDP20 and PBTDP25 degraded faster than PBTDPs with a lower ratio of pyrrolidone under enzymatic conditions, due to the improved hydrophilicity and reduced crystallinity of copolyesters themselves. Surprisingly, PBTDP20 and PBTDP25 were completely shattered after 10 days, while other specimens retained their entire frames.

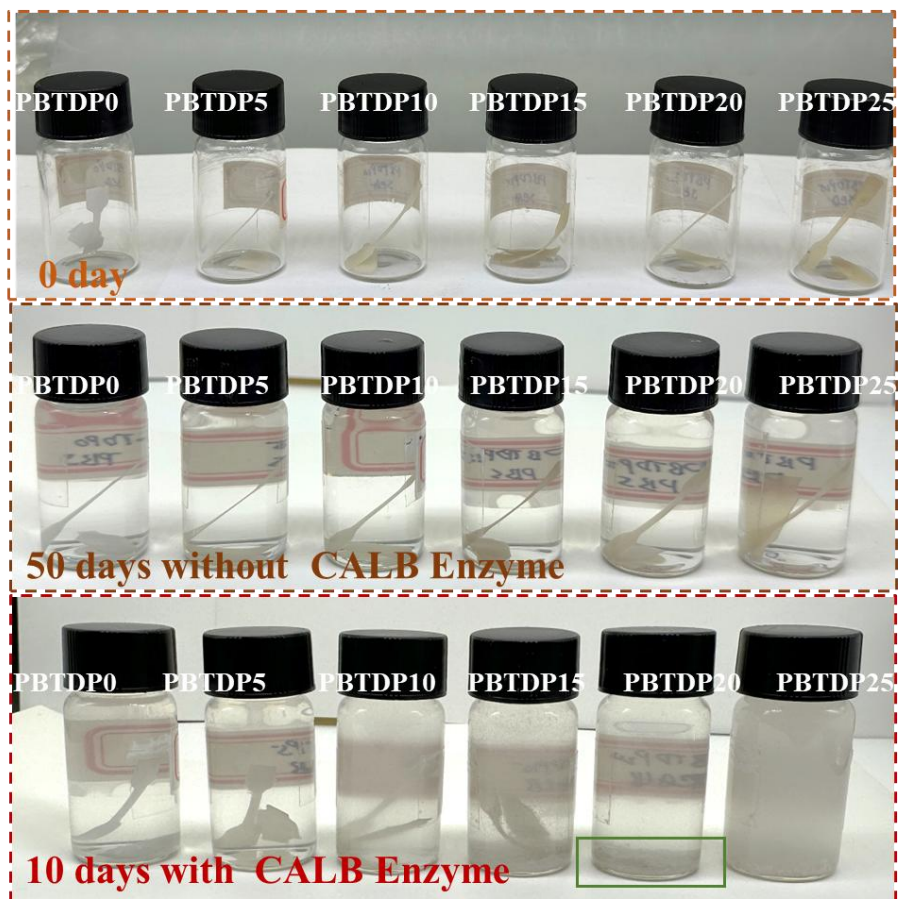


Figure: Macroscopic topography photos of PBTDPs before and after degradation experiments.

Reactive oxygen species (ROS) play a dual role in biological systems: they function as essential mediators in signal transduction and immune regulation, yet their excessive accumulation induces oxidative stress and contributes to various diseases. Hence, the development of functional polymers with controllable degradability and selective ROS responsiveness holds great promise for disease diagnosis and precision therapy. Furan-based polyesters derived from renewable feedstocks have attracted considerable

attention due to their stability and biocompatibility. However, their rigid backbones and slow degradation limit biomedical applications. Incorporating heteroatom-containing diacids and tuning copolymerization ratios can achieve controllable degradation, though the lack of ROS-specific responsiveness remains a challenge.

Here, PBFTd polyesters were designed with synergistic effects from furan rings and sulfur-containing chains, endowing them with excellent O₂, CO₂, and water vapor barrier properties. Upon H₂O₂ oxidation, the materials exhibited enhanced hydrophilicity and accelerated degradation, enabling controllable breakdown. The hydrolysis pathway was further elucidated by theoretical calculations, highlighting energy barrier variations and noncovalent interactions. These results demonstrate the potential of cell membrane-inspired polyesters for sustainable and biomedical applications.

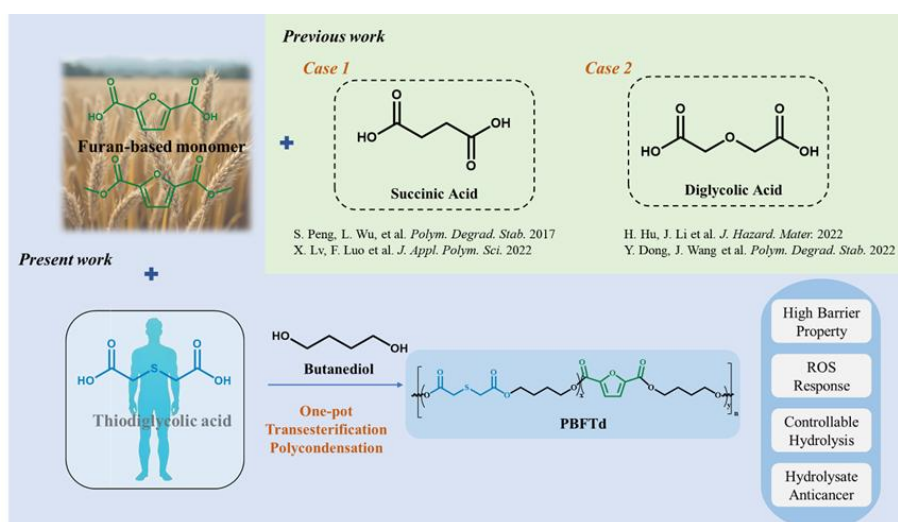


Figure: Scheme Synthesis of PBFTd.

Bio-based polyesters (such as FDCA-derived polymers) have demonstrated excellent thermal stability, mechanical strength, and biocompatibility, making them promising candidates for sustainable polymer applications. However, their rigid main chains lead to slow degradation rates and poor controllability. For example, PBF possesses favorable performance but remains difficult to achieve precise degradation under physiological or environmental conditions. Current strategies, such as PBSF copolyesters, enable biodegradation in composting or enzymatic environments but lack controllability in broader contexts. Similarly, PBDF copolyesters incorporating

DGA achieve controlled hydrolytic degradation but fail to provide responsiveness to reactive oxygen species (ROS). Meanwhile, typical ROS-responsive polymers such as PPS show limited structural versatility, complex synthesis, and potential biosafety concerns.

Inspired by the phospholipid bilayer of cell membranes, which regulates molecular transport via hydrophilic heads and hydrophobic tails, we introduced thiodiacetic acid (TDA)—a natural human metabolite with excellent biocompatibility and medical relevance—as a functional design unit. The thioether bond (-S-) in TDA can be oxidized by ROS (e.g., H_2O_2) into hydrophilic sulfoxide (-SO-) and sulfone (-SO₂-) groups, thereby endowing the polymer with ROS responsiveness. By copolymerizing TDA with rigid furan units derived from DMFD, we developed a novel copolyester, PBFTd. This design enables oxidation-triggered modulation of chain hydrophilicity, analogous to membrane-regulated molecular permeability, thereby controlling water access to ester bonds and tuning the hydrolytic degradation process.

This approach not only confers controllable degradation under ROS conditions but is also expected to maintain or even surpass the outstanding properties of FDCA-based polyesters, including high thermal stability and excellent barrier performance. The development of PBFTd opens new avenues for the functionalization and intelligent design of bio-based polyesters, with promising applications in degradable packaging and biomedical devices.

Hydrolytic and seawater degradation of PBFTd

The incorporation of aliphatic segments into aromatic polyesters shows enhanced hydrolytic degradability. Even hydrophilic structures that are not inherently degradable monomers—such as lactic acid, glycolic acid, diglycolic acid, and oxalic acid—can promote the degradation of aromatic polyesters. Dubois introduced succinic acid and adipic acid into PBF, and reported that aliphatic segments undergo hydrolysis more readily than aromatic segments, with amorphous domains degrading more rapidly than crystalline ones.

In contrast to the non-degradable nature of neat PBF, the incorporation of Td units disrupts crystallinity, facilitating water penetration and ester bond

cleavage in the amorphous regions, thereby imparting degradability. As shown in Figure, PBFTd with 10% Td units exhibit a 3% weight loss after 56 days in phosphate-buffered solutions. Increasing the Td contents to 60% results in a corresponding weight loss of 8%, indicating a composition-dependent degradation behavior.

The structural evolution of PBFTd samples after hydrolysis was further analyzed. As shown in Figure 6(b), the yellow region highlights the relative changes in Td units as determined by NMR spectroscopy. A consistent decrease in Td units were observed post-hydrolysis. Specifically, PBFTd samples with 10% and 20% Td units showed a 1% reduction, while the sample with 30% Td units exhibited a 2% decrease. More pronounced reductions were observed in samples containing 40, 50, and 60% Td units, with decreases of 3%, 6%, and 16%, respectively, indicating greater susceptibility of higher Td-content materials to hydrolytic cleavage. The green region illustrates changes in number average molecular weight (M_n) before and after hydrolysis. All PBFTd samples exhibited M_n reduction, consistent with chain scission during hydrolysis. The extent of degradation increased with Td units, with M_n decreasing by 1.5-fold in low Td contents sample and up to 3.8-fold in the sample containing 60% Td units.

The purple region shows the integrated area of the broad –OH stretching band at $3200\text{--}3600\text{ cm}^{-1}$ in the FTIR spectra, corresponding to free hydroxyl groups. A marked increase in the hydroxyl area after hydrolysis confirms the occurrence of ester bond cleavage. Moreover, the intensity of this increase correlated positively with Td content, further supporting the composition-dependent hydrolytic degradation behavior.

Despite the hydrolytic degradability of PBFTd, a comparison with previously reported degradable PBF-based copolyesters reveals its relatively slower degradation rate as shown in Figure 19 (c), PBFTd hydrolyzes more slowly than oxalic acid-modified PBOF and diglycolic acid-modified PBDF, both of which possess highly hydrophilic moieties. Even PBAF, modified with adipic

acid, showed slightly higher degradation efficiency than PBFTd. In contrast, the hydrolytic rate of PBFTd was found to be comparable to that of PBSF containing succinic acid units.

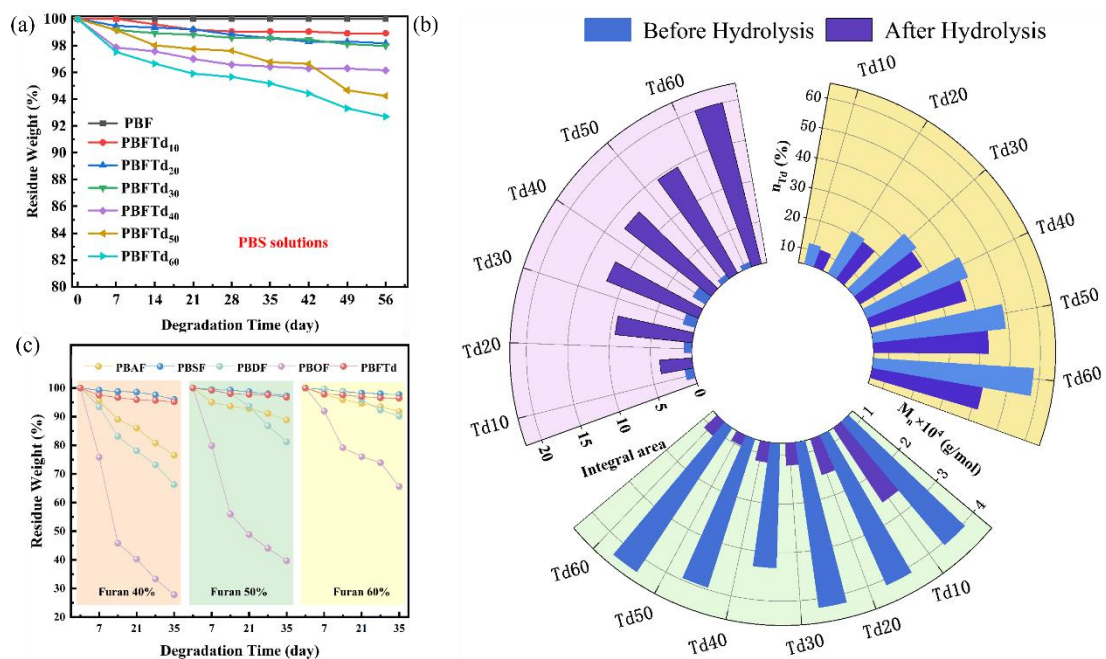


Figure: (a) Hydrolysis residue weight of PBFTd in PBS solutions over time. (b) The structure and molecular weight changes of PBFTd before and after 56 days of hydrolysis. (c) Comparison chart of hydrolysis of PBFTd with similar aliphatic modified-PBF and hydrophilic monomer modified-PBF.